Droplets in Microchannels: Dynamical Properties of the Lubrication Film

Axel Huerre,[1] Olivier Theodoly,[2] Alexander M. Leshansky,[3] Marie-Pierre Valignat,[2] Isabelle Cantat,[4] and Marie-Caroline Jullien[1]

[1]*MMN, UMR CNRS Gulliver 7083, PSL research University, ESPCI ParisTech, 10 rue Vauquelin, F-75005 Paris, France*

[2]*Laboratory Adhesion & Inflammation, Aix Marseille Université UM 61; Inserm UMR_S 1067; CNRS UMR 7333; Assistance Publique Hôpitaux de Marseille, 163 avenue de Luminy, 13009 Marseille, France*

[3]*Department of Chemical Engineering, Technion-IIT, Haifa 32000, Israel*

[4]*IPR, UMR CNRS 6251, Universite de Rennes 1, 35000 Rennes, France*

(Received 28 October 2014; revised manuscript received 22 April 2015; published 3 August 2015)

We study the motion of droplets in a confined, micrometric geometry, by focusing on the lubrication film between a droplet and a wall. When capillary forces dominate, the lubrication film thickness evolves nonlinearly with the capillary number due to the viscous dissipation between the meniscus and the wall. However, this film may become thin enough (tens of nanometers) that intermolecular forces come into play and affect classical scalings. Our experiments yield highly resolved topographies of the shape of the interface and allow us to bring new insights into droplet dynamics in microfluidics. We report the novel characterization of two dynamical regimes as the capillary number increases: (i) at low capillary numbers, the film thickness is constant and set by the disjoining pressure, while (ii) above a critical capillary number, the interface behavior is well described by a viscous scenario. At a high surfactant concentration, structural effects lead to the formation of patterns on the interface, which can be used to trace the interface velocity, that yield direct confirmation of the boundary condition in the viscous regime.

DOI: 10.1103/PhysRevLett.115.064501 PACS numbers: 47.55.D-, 47.15.gm, 47.55.dk, 47.55.N-

The dynamics of a droplet confined between solid walls and pushed by a surrounding liquid is an old problem; however, recent theories are still being developed to describe unexplored regimes and experimental characterizations are still lacking that shed light on these novel developments. A complete understanding of the droplet velocity calls for an accurate knowledge of the dissipation mechanisms involved, particularly in the lubrication film. Our understanding of the lubrication properties of menisci traveling in confined geometries has been steadily refined since the pioneering work of Taylor and Saffman [1]. Notably, the influence of the lubrication film left along the wall by the moving meniscus was first taken into account by Bretherton, who investigated the motion of an inviscid bubble in a cylindrical tube [2]. Far from the meniscus, this dynamical film reaches a uniform thickness h_∞, related to the bubble velocity through the capillary number $\mathrm{Ca} = \mu_f U_d/\gamma$, where U_d is the bubble velocity, μ_f is the viscosity of the continuous phase, and γ is the surface tension. When the capillary pressure dominates over the viscous stress, i.e., in the regime where $\mathrm{Ca} \ll 1$, the thickness of the film follows $h_{\mathrm{Breth}} = 1.34 r \mathrm{Ca}^{2/3}$, where r is the radius of the capillary tube. Besides bubbles, the case of viscous droplets remains however largely unexplored. A recent theoretical advance in the field by Hodges *et al.* [3] shows by numerical calculations of the whole flow pattern that significant corrections in the thickness of lubrication films can arise at very low Ca. Furthermore, the regime of the Bretherton theory is only valid for lubrication films thicker than the molecular sizes or than the range of interfacial interactions. The typical velocities and length scales involved in droplet-based microfluidics would lead to lubrication films $h_\infty \sim 7$–8 nm for oil-in-water droplets traveling at $100\ \mu\mathrm{m}\cdot\mathrm{s}^{-1}$ in $15\ \mu$m-deep channels. This is below the thickness of the common black film (i.e., the equilibrium film balancing electrostatic repulsion and van der Waals attraction, Derjaguin-Landau-Verwey-Overbeek theory), which is of about 20 nm for an aqueous phase containing sodium dodecyl sulfate (SDS) [4,5]. Experimental investigations of the dynamical properties of nanometric lubrication films, typically accessible at low Ca, are largely lacking [6,7].

Boundary conditions are of prime importance for the determination of the lubrication film thickness [8,9]. In this respect, three asymptotic regimes, corresponding to three boundary conditions at the interface, have been identified for bubbles. (i) In the stress-free case, the fast remobilization of surfactants in the outer phase leads to a perfectly compressible interface, as it would be without surfactants. Oppositely, (ii) the sliding case corresponds to an incompressible interface with identical interface and bubble velocities as in a solid case, $U_{\mathrm{int}} = U_d$ in the laboratory frame. (iii) In the rolling case $U_{\mathrm{int}} = 0$ and the interface is incompressible in the film; it is created and suppressed at the front and rear of the bubble, respectively. The scaling law is not affected by these different boundary conditions, but numerical prefactors are introduced in the expression for h_∞, which becomes h_{Breth}, $2^{2/3}h_{\mathrm{Breth}}$, or $4^{2/3}h_{\mathrm{Breth}}$,

respectively [9,10]. Moreover, the scaling law can be modified by the droplet viscosity. Considering the classical lubrication approach, Teletzke *et al.* showed that there is a transition for the prefactor from 1 to $2^{2/3}$ for viscosity ratio of about 10^3 [6]. Nevertheless, Hodges *et al.* [3] took into account the whole nontrivial flow pattern inside and outside the droplet to derive a thickness correction $\delta h_{\mathrm{visc}} = h_\infty - h_{\mathrm{Breth}}$ for a droplet with a viscosity contrast $\lambda = \mu_d/\mu_f = 25$, which verifies $\delta h_{\mathrm{visc}} = 8.68H\mathrm{Ca}$. Droplet viscosity thus leads to thicker films than the stress-free case in this scenario. In this Letter, we propose an unprecedented experimental analysis of lubrication films at low capillary numbers for viscous oil in water droplets stabilized by surfactants. A quantitative optical measurement of a lubrication film thickness as small as 20 nm and interface velocities allows us to shed new light on the low Ca regime, where both hydrodynamic and interfacial force effects are expected to yield unexplored deviations from the Bretherton theory. We expect these results, which shed new light on droplet dynamics, to be of broad interest in the rapidly growing research field of droplet-based microfluidics [11–14].

Oil-in-water droplets of radius $R = 55 \pm 2$ μm are generated at a T junction in a polydimethylsiloxane (Sylgard 184) microfluidic system [15,16], and enter a 2500×9000 μm Hele-Shaw cell of height $2H = 25 \pm 1$ μm. The outlet is directly punched in the cell, to avoid a pressure drop from a channel outlet that might induce deformation of the high-aspect-ratio cavity. The droplets are mineral oil (SIGMA 8042-47-5) in deionized water with SDS at 1.42 and 4.72 g/L [respectively, 0.6 and 2 times the critical micelle concentration (CMC)]. The surface tension between the two fluids is $\gamma = 1.6 \times 10^{-2}$ N/m at 0.6 times the CMC and $\gamma = 1 \times 10^{-2}$ N/m at 2 times the CMC. The viscosities are $\mu_f = 10^{-3}$ Pa · s for the aqueous solution and $\mu_d = 25 \times 10^{-3}$ Pa · s for the mineral oil, with a precision of 1×10^{-4} Pa · s. The oil droplets do not wet the walls of the cell so that there are no contact lines. We impose the water flow rate (Nemesys controller), ranging from 2 to 100 μL/ min. Corresponding droplet velocities vary between 50–5000 μm/s and capillary numbers vary between 6×10^{-6} and 5×10^{-4}. Lubrication film thicknesses are measured using reflection interface contrast microscopy [17,18]. The wavelength used is 550 nm, so that two successive extrema in the interference pattern correspond to a film thickness difference of about 130 nm, and the optical indexes used in the model are 1.515, 1.33, 1.467, and 1.412, respectively for the glass plate, water solution, mineral oil, and polydimethylsiloxane. The movies are acquired with a high speed camera (Photron Fastcam SA4) at a maximum frequency of 1000 Hz, which results in a maximum of six blurred pixels at the highest velocities. The pixel resolution is 0.6 μm; the pictures are normalized by the background without a droplet to get rid of spatial inhomogeneities in lighting. The thicknesses h_∞ of the wetting film reported in Figs. 2 and 3(a) are obtained by averaging the local thickness over a rectangular central zone where the film thickness is constant [see Fig. 1(b)] and over 15 successive frames. The error bars result from the quadratic sum of the statistical error (from the 15 frames), the model error (from the numerical aperture), and the reference error in the normalized intensity calculation. Details about the reflection interface contrast microscopy method and the error bar calculation are given in the Supplemental Material [19].

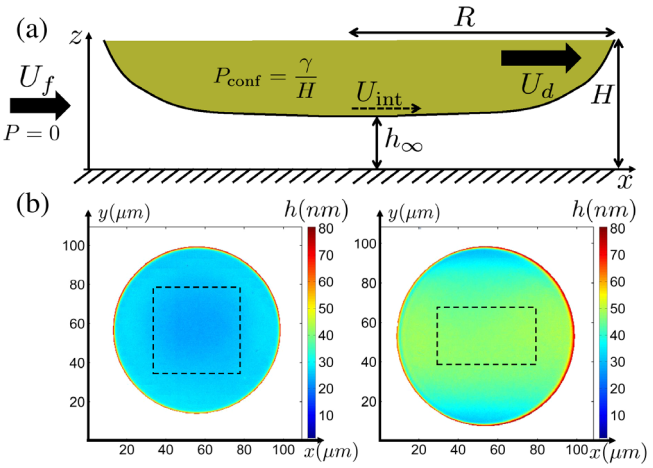

FIG. 1 (color online). (a) Schematics of the experiment and notations used in the text. (b) Left: plot of the film thickness for $\mathrm{Ca} = 3.1 \times 10^{-6}$. Right: plot of the film thickness for $\mathrm{Ca} = 8.1 \times 10^{-5}$. Dotted rectangles: averaging area for the mean film thickness h_∞.

The first set of experiments was performed below the CMC (0.6 times the CMC, i.e., 4.92 mM). Schematics and experimental topographies are shown in Fig. 1 to illustrate the geometry of the droplets. In particular, plots of the lubrication film thickness are given for two droplets flowing at different velocities, see Fig. 1(b) (the full 3D profiles are represented as videos in the Supplemental Material [19]). As the droplet velocity increases above $\mathrm{Ca} \sim 7 \times 10^{-5}$, the shape of the interface smoothly changes from a homogeneous film of constant thickness [$\mathrm{Ca} < 7 \times 10^{-5}$; Fig. 1(b), left] to a more complex 3D shape, while the film thickness at the center increases [$\mathrm{Ca} > 7 \times 10^{-5}$; Fig. 1(b), right]. Note that to our knowledge, no model so far has predicted the 3D shape of a flowing droplet in a Hele-Shaw cell: though the full characterization of these profiles is not the aim of this Letter, our results give a first picture of these complex shapes.

Measuring the film thickness h_∞ allows us to quantify the transition between two dynamical regimes as the capillary number increases, see Fig. 2. Above a critical capillary number $\mathrm{Ca}^* \sim 3 \times 10^{-5}$, the film thickness increases with the capillary number according to the

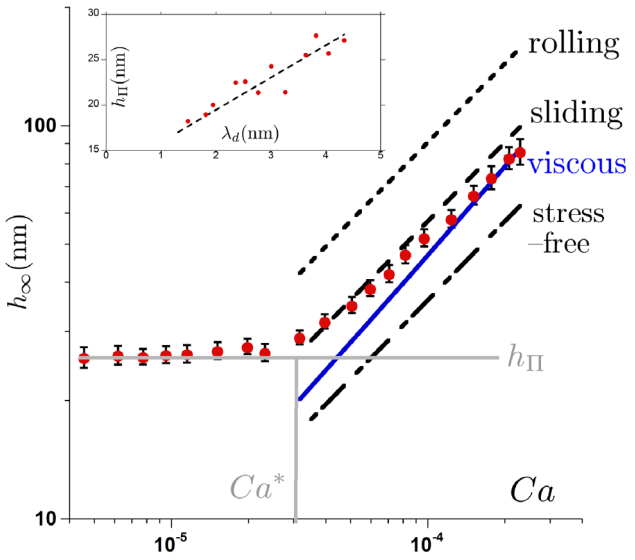

FIG. 2 (color online). Film thickness as a function of the capillary number. (red dots) Experimental data. Lines: theoretical predictions for different boundary conditions [10]: (dot-dashed) stress free, (dashed) sliding, (dotted) rolling. (solid blue) stress continuity at the interface with a viscous drop ($\mu_d/\mu_f = 25$) [3]. h_Π = static film thickness. Inset: static film thickness h_Π as a function of the Debye length λ_D.

Hodges *et al.* [3] theory, while below Ca^* it remains constant, in agreement with theoretical predictions by Teletzke *et al.* [6]. Indeed, at high velocities, the film thickness is governed by a balance between viscous entrainment and capillary suction; the film is thick enough for short range interactions to be negligible. At low velocities, the viscous entrainment is reduced, which results in thinner films where short range repulsive effects, represented by the disjoining pressure Π_{disj}, become dominant.

To further characterize the capillary regime $Ca > Ca^*$, we compare our data to theoretical predictions for different conditions at the interface: the stress-free case, the sliding case ($U_{\text{int}} = U_d$ in the laboratory frame), the rolling case ($U_{\text{int}} = 0$) [9,10], and the viscous model $\mu_f \partial u/\partial z = \mu_d \partial v/\partial z$ [3]. As seen above, these different conditions affect the numerical prefactor to Bretherton's scaling $h_\infty \propto H\text{Ca}^{2/3}$ for the first three boundary conditions, while for the viscous model there is an additional linear scaling in Ca. These predictions are plotted in Fig. 2 with no adjustable parameter, showing a quantitative agreement between our data and the theoretical curve for the viscous model $h_{\text{visc}} = h_{\text{Breth}} + \delta h_{\text{visc}} = 1.34H\text{Ca}^{2/3} + 8.68H\text{Ca}$ (see the Supplemental Material [19]) and the sliding model. We will show in the second part of the Letter that the interface velocity is negligible compared to the droplet viscosity, allowing us to finally discard the sliding regime. While sliding or stress-free motions have been previously reported [20], to our knowledge this is the first experimental observation of a viscous regime for droplets.

When the capillary number decreases below Ca^*, disjoining pressure effects become dominant and the lubrication film thickness reaches a plateau. This asymptotic value is consistent with the static film thickness $h_\Pi \sim 25$ nm measured for a droplet at rest ($U_d = 0$), which is set by the disjoining pressure γ/H (i.e., imposed by the confinement). In these experimental conditions, the disjoining pressure is governed by electrostatic effects rather than van der Waals or steric forces (common black film [21]; see the thick branch on the disjoining pressure isotherm in the Supplemental Material [19]). This is verified by the linear relation between the static film thickness h_Π and the Debye length $\lambda_D = 0.3/\sqrt{C_{\text{SDS}}(\text{mol/L})}$, see Fig. 2, inset. The Debye length was tuned down by adding NaCl up to 0.4 M, while the SDS concentration was adjusted to maintain 0.6 times the CMC [22].

Having investigated the electrostatic contribution of the disjoining pressure, experiments above the CMC were performed to explore the influence of structural effects.

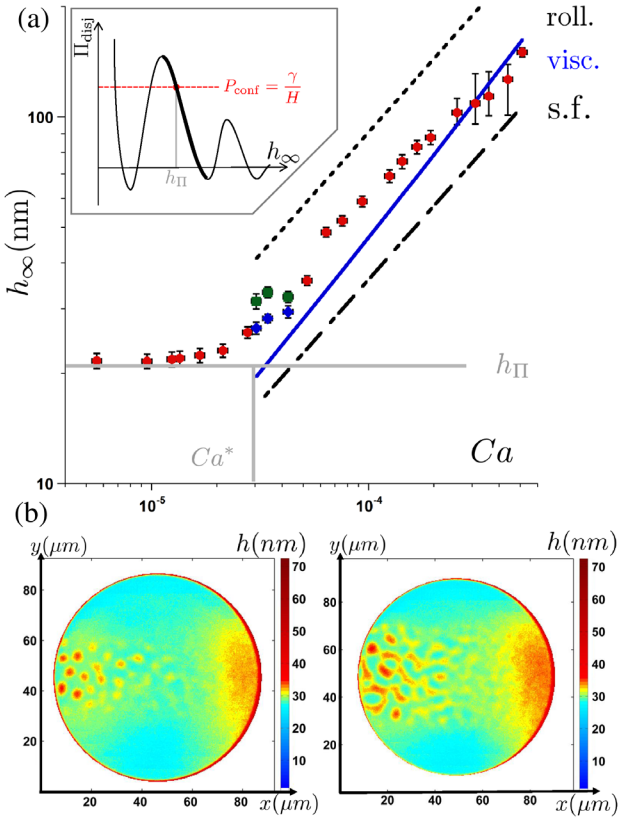

FIG. 3 (color online). (a) Local film thickness as a function of the capillary number. (red dots) Experimental data. For $3 \times 10^{-5} < \text{Ca} < 5 \times 10^{-5}$, two thicknesses coexist: (green squares) $h_{\max}$ and (blue lozenges) $h_{\min}$. Lines: see Fig. 2. Inset: sketch of the oscillatory disjoining pressure isotherm, according to a structural model [21]. The bold line corresponds to the common black film. (b) Spatial plot of the film thickness, for two capillary numbers in the transition zone (left, $\text{Ca} = 3 \times 10^{-5}$; right, $\text{Ca} = 3.4 \times 10^{-5}$). $h_{\max}$ is coded in red and $h_{\min}$ in light blue. Note that the color scales are adjusted in order to enhance the pattern contrast.

At 2 times the CMC, the evolution of the film thickness with Ca is qualitatively similar, but the plateau value below Ca^* is lower: $h_\Pi \sim 20$ nm, see Fig. 3(a). Indeed, increasing the SDS concentration decreases λ_D, and thus the equilibrium film thickness.

Another difference from the low surfactant concentration results is the coexistence of two distinct thicknesses, $h_{\min}$ and $h_{\max}$, at the transition between the two regimes [Fig. 3(a)].

The patterns visible in Fig. 3(b) are characteristic of a spinodal decomposition, sometimes involved in disjoining pressure-governed phenomena [4,23]. In micellar solutions, such a phenomenon is due to the oscillatory shape of the disjoining pressure isotherm, see the inset in Fig. 3(a) [4,5,21]. These oscillations stem from structural interactions between highly concentrated micelles, and have a wavelength equal to the effective micelle size, i.e., the diameter of a micelle plus twice the Debye length. Here, the difference $h_{\max} - h_{\min} \sim 6$ nm indeed corresponds to the size of a spherical SDS micelle and its water environment ($r_{\text{mic}} \sim 2$ nm, $\lambda_D = 2.3$ nm) [5], and is therefore consistent with a transition taking place between two successive branches of the isotherm.

These patterns can also be used to estimate the velocity of the interface. A spatiotemporal plot of the lubrication film thickness taken along a cross section of the droplet in the direction of motion is shown in Fig. 4(a). Such a picture

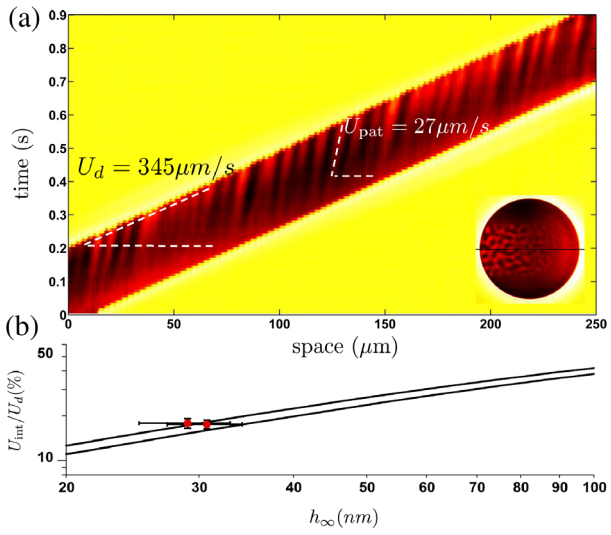

FIG. 4 (color online). (a) Spatiotemporal plot of a droplet cross section (raw interference patterns). The section is taken along the direction of movement, as shown in the inset. Brighter colors correspond to higher thicknesses, in arbitrary units. The droplet and pattern velocities are measured from the angles between the dashed white lines: $U_d = 345$ μm/s and $U_{\text{pat}} = 27$ μm/s. (b) Normalized interface velocity $(U_{\text{int}}/U_d) * 100$ as a function of the lubrication film thickness h_∞. (red dots) Experimental data. (solid line) Upper and lower estimations assuming a viscous model.

gives access to the droplet velocity U_d, deduced from the slope of the droplet edge, and to the pattern velocity U_{pat}. The film thickness fluctuations $h(x,t)$ are related to the interface velocity through the lubrication equations, leading to $U_{\text{pat}} = U_{\text{int}}/2$ (see the Supplemental Material [19] for a detailed calculation). We measured $U_{\text{pat}} = 27$ $\mu\text{m} \cdot \text{s}^{-1}$, i.e., $U_{\text{int}} = 54$ $\mu\text{m} \cdot \text{s}^{-1}$: the interface velocity is thus much smaller than the droplet velocity $U_d = 345$ $\mu\text{m} \cdot \text{s}^{-1}$, allowing us to disregard a sliding scenario.

We can now deduce the surface tension profile along the interface over the whole wetting film from the droplet and interface velocities. The stress balance at the interface is written $\partial\gamma/\partial x = \mu_f \partial u/\partial z - \mu_d \partial v/\partial z$. The normal velocity derivatives are taken from a parabolic profile inside the droplet and a simple shear profile in the film, assuming $h_\infty \ll H$. The stress balance is integrated over the film length $2(R-H)$ from the front to the rear of the droplet. This leads to $\Delta\gamma_{\text{film}} = [\mu_f U_{\text{int}}/h_\infty - 3\mu_d(U_d - U_{\text{int}})/H] \times 2(R-H)$, which we solve numerically to find a surface tension difference of $4 \times 10^{-6} \pm 3 \times 10^{-5}$ N/m for $\text{Ca} = 3.45 \times 10^{-5}$. This very low value allows us to disregard the influence of surface tension gradients on the dynamics. This confirms that the model for two immiscible pure liquids [3] provides a relevant description for our experiment, despite the presence of surfactants in the solution. Assuming this remains true over the whole range of capillary numbers, we can then predict the value of the interfacial velocity: $U_{\text{int}}/U_d = 1/[1 + H/(3\lambda h_\infty)]$. The upper and lower estimations (considering errors on λ and H) are plotted in Fig. 4(b). The experimental points for two different capillary numbers at the transition (where patterns are seen) are also plotted and lie between the two theoretical curves. Such quantitative data could prove useful to rationalize the complex behavior of the interface, though this would go beyond the scope of this Letter.

At high confinement, two regimes have been evidenced in the dynamical properties of the lubrication film between a traveling droplet and a solid wall. Two distinct regimes are evidenced: a capillary regime at large capillary numbers, as classically reported, and a regime governed by the disjoining pressure at lower capillary numbers. We expect this first experimental characterization of the disjoining pressure regime to open the way towards further work, such as the static or dynamical study of the disjoining pressure in a liquid-liquid-solid configuration. Two models have been discussed and characterized, showing the relevance of Teletzke *et al.*'s model in the disjoining regime [6] and the relevance of Hodges *et al.*'s model [3] in the capillary regime, the latter emphasizing the effect of droplet viscosity, even at a low viscosity ratio. These observations are of prime importance for the community and should impact research focused more generally on diphasic flows at the microscales. Moreover, measuring the complete topography of the lubrication film uncovered new fundamental information: at high capillary numbers, the lubrication film

adopts a complex catamaranlike shape (see the movie in the Supplemental Material [19]), which should prove of interest for 3D modeling. For intermediate capillary numbers, above the CMC, a spinodal decomposition gives access to interfacial properties that evidence a complex viscous behavior; these experiments will pave the way towards the study of more complex situations, such as the influence of nonsoluble surfactants and its competition with viscosity.

This work was supported by CNRS, IPGG (Equipex ANR-10-EQPX-34), ESPCI, ANR under Contract No. 13-BS09-0011-01, and INSERM. A. M. L. acknowledges the support of the Israel Science Foundation (ISF) via Grant No. 1319/09 and a Joliot Chair visiting position at Ecole Supérieure de Physique et Chimie de Paris (ESPCI). We acknowledge valuable discussions with Michael Schindler and Cécile Monteux.

[1] G. Taylor and P. G. Saffman, Q. J. Mech. Appl. Math. **12**, 265 (1959).
[2] F. Bretherton, J. Fluid Mech. **10**, 166 (1961).
[3] S. R. Hodges, O. E. Jensen, and J. M. Rallison, J. Fluid Mech. **501**, 279 (2004).
[4] A. Nikolov and D. Wasan, J. Colloid Interface Sci. **133**, 1 (1989).
[5] V. Bergeron and C. J. Radke, Langmuir **8**, 3020 (1992).
[6] G. F. Teletzke, H. T. Davis, and L. Scriven, Rev. Phys. Appl. **23**, 989 (1988).
[7] J.-D. Chen, J. Colloid Interface Sci. **109**, 341 (1986).
[8] A. Huerre, V. Miralles, and M.-C. Jullien, Soft Matter **10**, 6888 (2014).
[9] I. Cantat, Phys. Fluids **25**, 031303 (2013).
[10] A. Q. Shen, B. Gleason, G. H. McKinley, and H. A. Stone, Phys. Fluids **14**, 4055 (2002).
[11] C. N. Baroud, F. Gallaire, and R. Dangla, Lab Chip **10**, 2032 (2010).
[12] N. Champagne, R. Vasseur, A. Montourcy, and D. Bartolo, Phys. Rev. Lett. **105**, 044502 (2010).
[13] I. Shani, T. Beatus, R. H. Bar-Ziv, and T. Tlusty, Nat. Phys. **10**, 140 (2014).
[14] H. A. Stone and S. Thutupalli, Nat. Phys. **10**, 87 (2014).
[15] Y. Xia and G. M. Whitesides, Annu. Rev. Mater. Sci. **28**, 153 (1998).
[16] V. van Steijn, C. R. Kleijn, and M. T. Kreutzer, Phys. Rev. Lett. **103**, 214501 (2009).
[17] A. S. G. Curtis, J. Cell Biol. **20**, 199 (1964).
[18] O. Theodoly, Z.-H. Huang, and M.-P. Valignat, Langmuir **26**, 1940 (2010).
[19] See Supplemental Material at http://link.aps.org/supplemental/10.1103/PhysRevLett.115.064501 for a definition of the common black film, details on the boundary conditions for viscous droplets, derivation of $U_{\mathrm{int}} = 2U_{\mathrm{pat}}$, optical model and error calculations and finally a summary movie with full topography maps.
[20] N. D. Denkov, S. Tcholakova, K. Golemanov, V. Subramanian, and A. Lips, Colloids Surf. A **282**, 329 (2006).
[21] V. Bergeron, J. Phys. Condens. Matter **11**, R215 (1999).
[22] R. J. Williams, J. N. Phillips, and K. J. Mysels, Trans. Faraday Soc. **51**, 728 (1955).
[23] M. L. Pollard and C. J. Radke, J. Chem. Phys. **101**, 6979 (1994).